Mathematical Investigation of Fluid Flow, Mass Transfer, and Slag-steel Interfacial Behavior in Gas-stirred Ladles

QING CAO and LAURENTIU NASTAC

In this study, the Euler-Euler and Euler-Lagrange modeling approaches were applied to simulate the multiphase flow in the water model and gas-stirred ladle systems. Detailed comparisons of the computational and experimental results were performed to establish which approach is more accurate for predicting the gas-liquid multiphase flow phenomena. It was demonstrated that the Euler-Lagrange approach is more accurate than the Euler-Euler approach. The Euler-Lagrange approach was applied to study the effects of the free surface setup, injected bubble size, gas flow rate, and slag layer thickness on the slag-steel interaction and mass transfer behavior. Detailed discussions on the flat/non-flat free surface assumption were provided. Significant inaccuracies in the prediction of the surface fluid flow characteristics were found when the flat free surface was assumed. The variations in the main controlling parameters (bubble size, gas flow rate, and slag layer thickness) and their potential impact on the multiphase fluid flow and mass transfer characteristics (turbulent intensity, mass transfer rate, slag-steel interfacial area, flow patterns, *etc*.,) in gas-stirred ladles were quantitatively determined to ensure the proper increase in the ladle refining efficiency. It was revealed that by injecting finer bubbles as well as by properly increasing the gas flow rate and the slag layer thickness, the ladle refining efficiency can be enhanced significantly.

I. INTRODUCTION

DURING ladle refining, argon stirring is commonly used to transport species to and away from the slag-steel interface, to homogenize the temperature and the composition of the molten alloy and to promote the slag-steel interaction, thus creating a large slag-steel interface to promote chemical reactions. Both the slag-steel interfacial area (A) and the mass transfer coefficient within the steel (k_m) are the main limiting factors for the desulfurization reaction kinetics in argon-stirred ladles.[1,2] The desulfurization rate is proportional to the product of A and k_m, known as the volumetric mass transfer coefficient (Ak_m).[3] The accurate prediction of the fluid flow and the slag-steel interaction characteristics in the ladle metallurgical furnace (LMF) is the foundation to study the desulfurization kinetics.

Since the temperature of the melt in LMF is typically above 1800 K, it is almost impossible to measure the actual interfacial area and the turbulent flow in gas-stirred ladles during plant operations. Over the past decades, the fluid flow phenomena in the gas-stirred ladle system were extensively investigated by using water model experiments and numerical simulations.[4–6] Computational fluid dynamics (CFD) modeling is considered as the most effective way to predict the turbulent flow and the slag-steel interface in gas-stirred ladles. The multiphase models[7–9] are widely used to predict the gas-liquid multiphase flow in a gas-stirred ladle, and they can be separated into the Euler-Lagrange approach and the Euler-Euler approach depending on how the gas phase is treated.[5,10]

The Lagrangian discrete phase model (DPM) in ANSYS Fluent is based on the Euler-Lagrange approach. In the Euler-Lagrange approach, the fluid phase is treated as a continuum by solving the Navier-Stokes equations. The mass and momentum conservation equations are solved only for liquid phase in an Eulerian frame of reference. The discrete phase is treated as individual particles or bubbles, and their trajectories are described by integrating the force balance on the particle under a Lagrangian frame of reference.[11,12] The interphase forces are taken into account through the momentum source term.[5,13,14] The Euler-Lagrange approach is also economical on computational resources.[15,16] The volume of fluid (VOF)

QING CAO and LAURENTIU NASTAC are with the Department of Metallurgical and Materials Engineering, The University of Alabama, Box 870202, Tuscaloosa, AL, 35487. Contact e-mail: lnastac@eng.ua.edu

model is based on the Euler-Euler approach. In this approach, different phases are treated mathematically as non-interpenetrating continua and the equations of conservation of mass and momentum are solved separately for each phase. The interfaces between phases are tracked exactly.[17]

VOF model has been widely used to study the fluid flow in gas-stirred ladle systems.[18–20] Petri Sulasalmia et al.[21] developed a multiphase VOF model to simulate slag entrainment and to track the interface between the slag and the steel based on water model experiments. Later, Liu et al.[22] and Li et al.[23] used the multiphase VOF method to simulate the transient three-dimensional and three-phase flow in LMF as well as the behavior of the slag layer. The fluctuant slag surface was simulated as well. Their simulation results showed that the injection flow rate of the argon gas has an effect on the spout height.[8,24]

It was found in the experiments that the gas injected into the liquid is dispersed as discrete bubbles.[5] Thus, many researches proposed to employ the Lagrangian DPM in describing the bubble plumes in gas-stirred ladles. Cloete et al.[17] developed a mathematical model by using the Lagrangian DPM to simulate the injected argon bubbles and the Eulerian multiphase VOF model for tracking the interface of the slag/steel phases. One major limitation of their work is that the unsteady fluctuation of the slag layer was not taken into account because of the assumption of the flat liquid surface. Then, Li et al.[25] developed a DPM-VOF coupled model to consider the dynamic free surfaces among liquid steel/slag/air phases.

One of the most crucial challenges of modeling multiphase fluid flow in LMF is the interaction between the injected gas and the continuous liquid, as well as the slag layer fluctuation. Although both Euler-Euler and Euler-Lagrange approaches have been applied in simulating gas-stirred ladle system, which model has better accuracy is still unclear. The effects of the gas stirring rate, injected bubble size, and other operating parameters on the turbulent flow and mass transfer in LMF is not thoroughly clarified. A significant amount of research has to be performed to further understand the complex phenomena that occur in gas-stirred ladles. In this study, the Euler-Euler and Euler-Lagrange approaches have been applied to simulate the multiphase flow in water model and gas-stirred ladle systems. The prediction accuracy of these two approaches has been investigated and compared. The effects of the gas stirring rate, injected bubble size, and slag layer thickness on the slag-steel interaction, slag eye evolution, and mass transfer coefficient were studied in detail.

II. OVERVIEW OF THE CFD MODELS

A. Euler-Euler Approach

In this approach, the multiphase VOF method is applied to simulate the transient three-dimensional air/water flow in a water cylinder, and argon gas/steel/slag/air four-phase fluid flow in an LMF.

The VOF formulation relies on the fact that two or more fluids (or phases) are not interpenetrating. For each additional phase that is added to the model, a variable is introduced, which represent the volume fraction of the phase in the computational cell. In each control volume, the volume fractions of all phases sum to unity. The tracking of the interfaces among phases is accomplished by solving the continuity equation for the volume fraction of phases. The continuity equation for the q_{th} phase is described in the following form:[7,25]

$$\frac{1}{\rho_q}\left[\frac{\partial}{\partial t}\left(\alpha_q \rho_q\right) + \nabla \cdot \left(\alpha_q \rho_q \vec{u_q}\right)\right] = 0, \qquad [1]$$

where the volume fraction α_q is constrained by $\sum_{q=1}^{n} \alpha_q = 1$.

The momentum equation is solved throughout the domain, and the resulting velocity field is shared among the phases. The momentum equation expressed as Eq. [2] is dependent on the volume fractions of all phases.

$$\frac{\partial}{\partial t}(\rho \vec{v}) + \nabla \cdot (\rho \vec{v}\vec{v}) = -\nabla p + \nabla \cdot \left[\mu\left(\nabla \vec{v} + \nabla \vec{v}^T\right)\right] + \rho \vec{g},$$
$$[2]$$

where ρ and μ are the density and viscosity, respectively, of the mixture depending on the volume fraction α_q of each phase. $\vec{v}$ is the underlying velocity field and p is the local pressure.

B. Euler-Lagrange Approach

In this approach, the VOF model is used for describing continuous phases (slag, steel, and air phases) and tracking the interfaces among phases. The interfaces are captured by the geo-reconstruct scheme, and the area of the slag-steel interface is computed and recorded every time step during the simulation. The blowing gas is treated as a discrete phase by injecting a stream of gas bubbles into the continuous phase.

The trajectory of each bubble is calculated in each time step according to force balance of the drag force, buoyancy force, virtual mass force, and the pressure gradient force.

$$\frac{d\vec{u_p}}{dt} = F_D\left(\vec{u} - \vec{u_p}\right) + \frac{\vec{g}(\rho_p - \rho)}{\rho_p} + \vec{F}_{vm} + \vec{F}_P. \qquad [3]$$

The four terms on the right represent the contributions of drag force, gravity, virtual mass, and pressure gradient force to particle acceleration. F_D is written as

$$F_D = \frac{18\mu}{\rho_p d_p^2} \frac{C_D Re}{24}. \qquad [4]$$

The virtual mass force, which would accelerate the fluid surrounding the bubble, is expressed as

$$\vec{F}_{vm} = C_{vm}\frac{\rho}{\rho_p}\left(\vec{u_p}\nabla\vec{u} - \frac{d\vec{u_p}}{dt}\right). \qquad [5]$$

The force that comes from the pressure gradient in the fluid is described as

$$\vec{F}_P = \frac{\rho}{\rho_p} \vec{u}_p \nabla \vec{u}. \qquad [6]$$

Here, $\vec{u}$ is the fluid phase velocity; $\vec{u}_p$ is bubble velocity; ρ is the fluid density; ρ_p is the density of the bubble; μ is the viscosity of the fluid, and d_p is the bubble diameter. Re is the relative Reynolds number. C_{vm} is the virtual mass factor with a default value of 0.5. The drag coefficient, C_D, is calculated as a function of bubble shape by using Eotvos number:[17]

$$C_D = \frac{2}{3} \left(\frac{E_0}{3} \right)^{0.5} \qquad [7]$$

$$E_0 = \frac{g(\rho - \rho_p)d_p^2}{\sigma}, \qquad [8]$$

where Eotvos number, E_0, is a dimensionless number describing the shape of the bubble. σ is the surface tension between the steel and the gas.

Turbulent dispersion creates a random addition to the liquid velocity for the drag force in Eq. [3]. It results in a wider bubble plume. Discrete random walk model is applied to account for the effects of turbulent dispersion on bubbles. Two-way turbulence coupling is implemented between the discrete and the continuous phases to facilitate momentum transfer between the bubbles and the continuous phases.

The collision, coalescence, and breakup phenomena of bubbles are included in this model. The algorithm of O'Rourke[26] is used to describe the coalescence process of the bubbles. Bubbles are considered to coalescence if they collide head-on, or to bounce if the collision is more oblique. The probability of coalescence can be related to the offset of the collector bubble center and the trajectory of the smaller bubble. And the critical offset is a function of the collisional Weber number and the relative radii of the collector (r_1) and the smaller bubble (r_2):

$$b_{crit} = (r_1 + r_2) \sqrt{\min \left(1.0, \frac{2.4f}{W_e} \right)}, \qquad [9]$$

where f is a function of r_1/r_2, defined as

$$f\left(\frac{r_1}{r_2} \right) = \left(\frac{r_1}{r_2} \right)^3 - 2.4 \left(\frac{r_1}{r_2} \right)^2 + 2.7 \left(\frac{r_1}{r_2} \right). \qquad [10]$$

The bubble breakup model proposed by Cloete et al.[17] is applied in the present model, which assumes that when the bubble diameter is over a critical diameter of 40 mm, two bubbles with equivalent mass are generated from one mother bubble. A more sophisticated bubble expansion and breakup model[13] can be used in a future study. The bubbles will disappear and join to the air to be a continuum after arriving to the liquid surface; thus, the present model removes the bubbles when they arrive to a position where the air volume fraction is above 0.5.

C. Turbulence Model

The realizable k-ε turbulence model is chosen to account for multiphase turbulence flow in both of the above-described CFD models. The standard wall functions are used as near-wall treatments for wall-bounded turbulent flows.[27]

The following transport equations for k and ε are solved:

$$\frac{\partial}{\partial t}(\rho k) + \frac{\partial}{\partial x_j}(\rho k u_j) = \frac{\partial}{\partial x_j} \left[\left(\mu + \frac{\mu_t}{\sigma_k} \right) \frac{\partial k}{\partial x_j} \right] + G_k + G_b - \rho\varepsilon \qquad [11]$$

$$\frac{\partial}{\partial t}(\rho\varepsilon) + \frac{\partial}{\partial x_j}(\rho\varepsilon u_j) = \frac{\partial}{\partial x_j} \left[\left(\mu + \frac{\mu_t}{\sigma_\varepsilon} \right) \frac{\partial \varepsilon}{\partial x_j} \right]$$
$$+ \rho C_1 S\varepsilon - \rho C_2 \frac{\varepsilon^2}{k + \sqrt{v\varepsilon}} + C_{1\varepsilon}\frac{\varepsilon}{k}C_{3\varepsilon}G_b, \qquad [12]$$

where

$$C_1 = \max\left[0.43, \frac{\eta}{\eta + 5} \right], \ \eta = S\frac{k}{\varepsilon}, \ S = \sqrt{2S_{ij}S_{ij}}, \text{ and}$$

$$S_{ij} = \frac{1}{2}\left(\frac{\partial u_j}{\partial x_i} + \frac{\partial u_i}{\partial x_j} \right).$$

In these equations, G_k represents the generation of turbulence kinetic energy due to the mean velocity gradient, calculated as

$$G_k = -\rho\overline{u_i' u_j'}\frac{\partial u_j}{\partial x_i}. \qquad [13]$$

G_b is the generation of turbulence kinetic energy due to buoyancy, calculated as

$$G_b = \beta g_i \frac{\mu_t}{Pr_t}\frac{\partial T}{\partial x_i}, \qquad [14]$$

where Pr_t is the turbulent Prandtl number for energy, which is 0.85 for the realizable k-ε model. g_i is the component of the gravitational vector in the th direction. The coefficient of thermal expansion, β, is defined as

$$\beta = -\frac{1}{\rho}\left(\frac{\partial\rho}{\partial T} \right)_P. \qquad [15]$$

The eddy viscosity, μ_t, is computed from

$$\mu_t = \rho C_\mu \frac{k^2}{\varepsilon}. \qquad [16]$$

The degree to which ε is affected by the buoyancy is determined by the constant $C_{3\varepsilon}$, which is calculated according to the following relation:

$$C_{3\varepsilon} = \tanh\left| \frac{v}{u} \right|, \qquad [17]$$

where v is the component of the flow velocity parallel to the gravitational vector and u is the component of the flow velocity perpendicular to the gravitational vector.

The model constants are $C_{1\varepsilon} = 1.44$, $C_2 = 1.9$, $\sigma_k = 1.0$, $\sigma_\varepsilon = 1.2$. C_μ is a function of the turbulence fields, as described in Reference 27.

The mass transfer coefficient in steel, k_m, can be calculated through the Kolmogorov theory of isotropic turbulence as follows:

$$k_m = cD_m^{0.5}\left(\frac{\varepsilon_l}{v_l}\right)^{0.25}, \qquad [18]$$

where c is a constant that is 0.4 for this study.[28] D_m represents the diffusion coefficient of the species in liquid steel as described by Lou et al.[28] ε_l is the turbulent energy dissipation rate and v_l is the kinematic viscosity.

D. Initial and Boundary Conditions

The meshed geometry of the LMF is shown in Figure 1. Initially, the slag layer rests on the top of the steel bath, and no argon blows through the plugs. Non-slip conditions with the standard wall function are employed at the bottom and the side walls. The pressure outlet boundary condition is used at the top surface of the ladle, where the argon gas are allowed to escape. The velocity inlet is used for the gas flow at the bottom plugs. The inlet velocity, u_b, is calculated in terms of the gas flow rate, Q.[27]

For the Lagrangian DPM, the number of injected bubbles per second (n) is calculated by using the gas flow rate and the injected bubble size:

$$n = \frac{6Q}{\pi d_{p,0}^3}. \qquad [19]$$

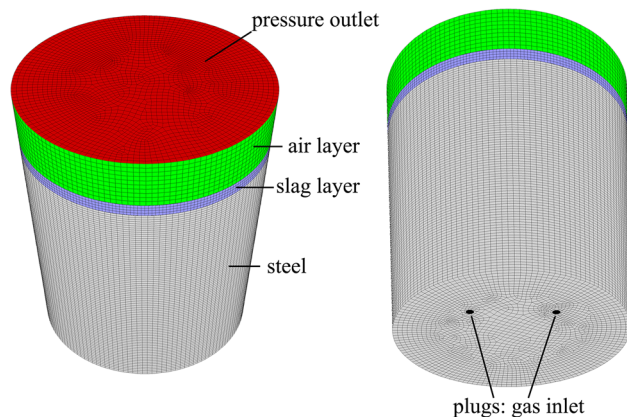The injected bubble size, $d_{p,0}$, is determined by the following equation:[13]

Fig. 1—The mesh geometry of the ladle furnace.

$$d_{p,0} = 0.091\left(\frac{\sigma}{\rho}\right)^{0.5} u_b^{0.44}. \qquad [20]$$

Table I shows the number of the injected bubbles per second under different gas flow rates and the injected bubble size in the DPM simulation studies. It can be seen that the number of bubbles included in the simulation studies is quite large. The computational cost of tracking all of the particles individually is prohibitive. Therefore, in ANSYS Fluent, the DPM model tracks a number of 'parcels', and each parcel is a representative of a fraction of the total mass flow released in a time step. The trajectory of each parcel is determined by tracking a single representative particle in the parcel.[16]

E. Numerical Procedure

The computation is carried out by using a transient pressure-based solver. The PISO scheme available in ANSYS Fluent is used for the pressure-velocity coupling and the volume fraction equation is solved using an explicit geo-reconstruct scheme.[16] The pressure staggering option (PRESTO!) scheme is selected for the pressure equation. A mesh sensitivity analysis for the VOF model has been conducted by using three different meshes, which correspond with the number of control volume elements of 239,000, 370,000, and 475,000. It was found that the meshes with 370,000 and 475,000 elements produced quite similar simulation results (such as the open slag eyes, slag-steel interface, and velocity distribution inside the ladle). Thus, the mesh with 370,000 elements is suitable for the current numerical simulation studies.

F. Model Validation

The prediction accuracy of the Euler-Euler and Euler-Lagrange approaches was investigated by comparing the simulated flow characteristics with the experimental results of a water model measured by Sheng et al.[29] The detailed study of the LMF operation simulation was conducted in an industry-scale ladle. The argon gas is supplied through two off-centered plugs at the bottom of the ladle. The ladle dimensions and thermo-physical properties of the steel and the slag are shown in Table II.

III. RESULTS AND DISCUSSIONS

A. Model Validation

In this section, the simulation results of the water model obtained by the Euler-Euler and the Euler-Lagrange approaches with a non-flat free surface, as well as the Euler-Lagrange approach with a flat free surface, are compared with the experimental data from Reference 29. For convenience, in the following discussion, the VOF model is used for representing the Euler-Euler

Table I. The Number of the Injected Bubbles Per Second Under Different Gas Flow Rates and Injected Bubble Size Used in the Simulation Studies

Q (L/s)	4	8	12	16	20	24	24	24	24
$d_{p,0}$ (mm)	1	1	1	1	1	1	5	10	15
n ($\times 10^5$/s)	76.43	152.87	229.30	305.73	382.17	458.60	3.67	0.46	0.14

Table II. The Dimensions of the Ladle and Other Parameters Employed in the Models

Diameter of Ladle (Up)	3100 mm
Diameter of Ladle (Down)	2660 mm
Height of Ladle	3500 mm
Argon Gas Flow Rate	4 to 24 L/s
Thickness of Slag	100 to 150 mm
Density of Liquid Steel	7020 kg/m^3
Density of Slag	3500 kg/m^3
Density of Argon	0.568 kg/m^3
Diffusion Coefficient of Species in Steel	7.0×10^{-9} m^2/s
Diameter of the Two Off-centered Plugs	0.092 m
Viscosity of Slag	0.03 kg/(m s)
Viscosity of Steel	0.006 kg/(m s)
Viscosity of Argon	2.125×10^{-5} kg/(m s)
Interfacial Tension Between Steel and Slag	1.15 N/m
Interfacial Tension Between Steel and Gas	1.4 N/m

approach and the DPM model is applied to represent the Euler-Lagrange approach.

Figure 2 shows the comparisons of the computed and the measured velocity and turbulent kinetic energy variations along the centerline of the gas inlet and in the radial direction. The comparison between the VOF and the DPM models indicates that the VOF model predicts quite high axial liquid velocity and turbulent kinetic energy near the gas inlet ($z < 0.025$ m). Above the gas inlet ($z > 0.025$ m), both the VOF and the DPM models predict well the axial liquid velocity along the centerline. The turbulent kinetic energy is underestimated by the DPM model, and more largely underestimated by the VOF model along the centerline. Along the radial line [see Figures 2(c) and (d)], there is an obvious discrepancy between the experimental and the simulated results. The DPM model predicts well the axial liquid velocity near the center region ($r < 0.05$ m) and the turbulent kinetic energy outside the center region ($r > 0.05$ m). Both VOF and DPM models underestimate the turbulent kinetic energy near the center region ($r < 0.05$ m). The VOF model largely underpredicts the axial liquid velocity and overestimates the turbulent kinetic energy outside the center region ($r > 0.05$ m). These comparison results demonstrate that the DPM is more accurate than the VOF model for the simulation of fluid flow characteristics in gas-stirred ladles. In addition, the Lagrange DPM model seems more economical on computational resources, since, in this study, the computational time required for a typical simulation time of 100 seconds using the Euler-Lagrange approach is shorter than that using the Euler-Euler approach by using the same number of CPU cores.

The free surface is a very complex and crucial region where spouts and fluctuating waves occur with turbulent dissipation. The setup of the liquid surface has significant influence on the model accuracy. In this study, the difference between the flat and the non-flat free surface setup is investigated and compared by using the DPM model. Figure 2(b) shows that the turbulent kinetic energy is sharply reduced to almost zero at the flat free surface and overestimated immediately below the flat free surface. Figures 2(c) and (d) indicate that the axial liquid velocity is largely underestimated near the wall, while turbulent kinetic energy is overestimated along the radial line when assuming a flat free surface. The reason is that when the free surface is flat, the dissipation of kinetic energy by wave production is ignored.[29] These results demonstrate that the flat free surface assumption can obviously affect the simulation accuracy. Thus, to properly simulate the turbulence near the free surface region, fluctuant waves must be allowed in the CFD model.

The validation of the bubble size distribution is carried out by comparing the simulation results with the experimental data measured by Li in a water model.[30] The predicted time-averaged bubble diameter evolution along the centerline of the plug is compared with the experimental data, as shown in Figure 3. The results are in reasonably good agreement, and therefore the present model can be used to describe the bubble plume in the gas-stirred system.

B. Comparison of Euler-Euler and Euler-Lagrange Approaches for Gas-stirred Ladles

The Euler-Euler and Euler-Lagrange approaches were applied to simulate the fluid flow and the slag-steel phase interaction behavior in industrial gas-stirred ladles. For the Euler-Euler approach, the argon gas/steel/slag/air four-phase VOF model was used. In
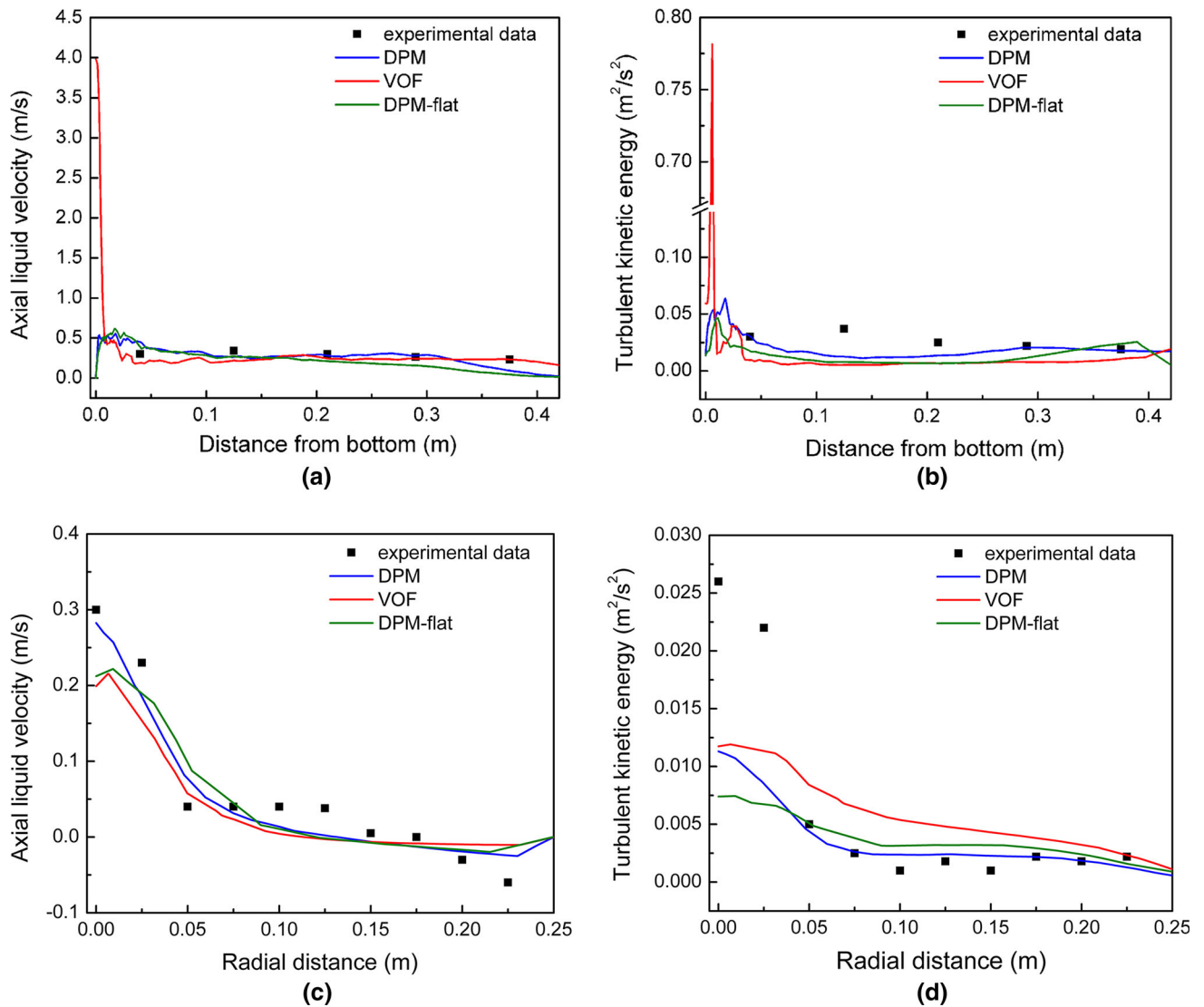
Fig. 2—Comparison of model predictions with Sheng and Irons's measurements (Ref. [29]), air flow rate = 50 mL/s: (*a*) the axial liquid velocity and (*b*) the turbulent kinetic energy along the plume centerline; (*c*) the axial liquid velocity, and (*d*) the turbulent kinetic energy along the radial direction at 0.21 m from the bottom.

addition, the Euler-Lagrange approach was applied by employing the DPM to describe the argon bubble plume and the VOF model for tracking the interface of the molten steel, slag, and air phases in the ladle. The gas flow rate is 24 L/s and the slag layer thickness is 150 mm. The predicted results of these two different models were compared.

Figure 4 shows the argon gas floating and the slag eye formation process at the beginning of the gas stirring. The upwelling gas in the VOF model is continuous and concentrated. While in the DPM model, the floating gas bubbles are dispersive and random. The size of the slag eyes is similar in both CFD models, while the fluctuation behavior of the top slag layer in the DPM model is stronger. A comparison of the simulated open slag eyes in the ladle against the industrial observation can be found in a previous study,[31] which indicates that the simulated open-eye size is in good agreement with the experimental observation.
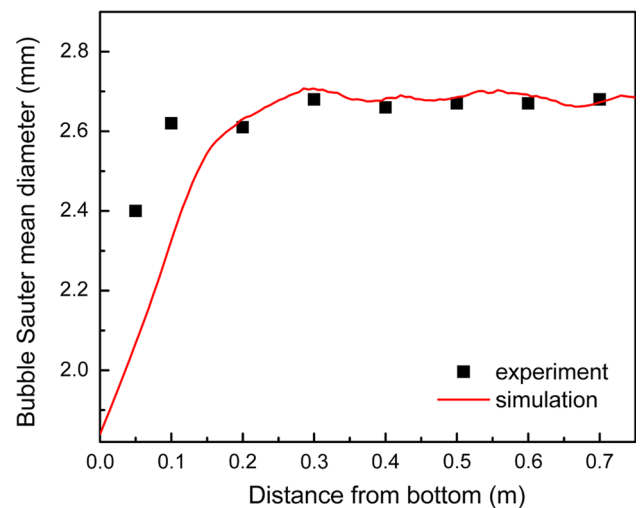

Fig. 3—Comparison of the bubble diameter evolution along the plug centerline between experiment (Ref. [30]) and simulation.
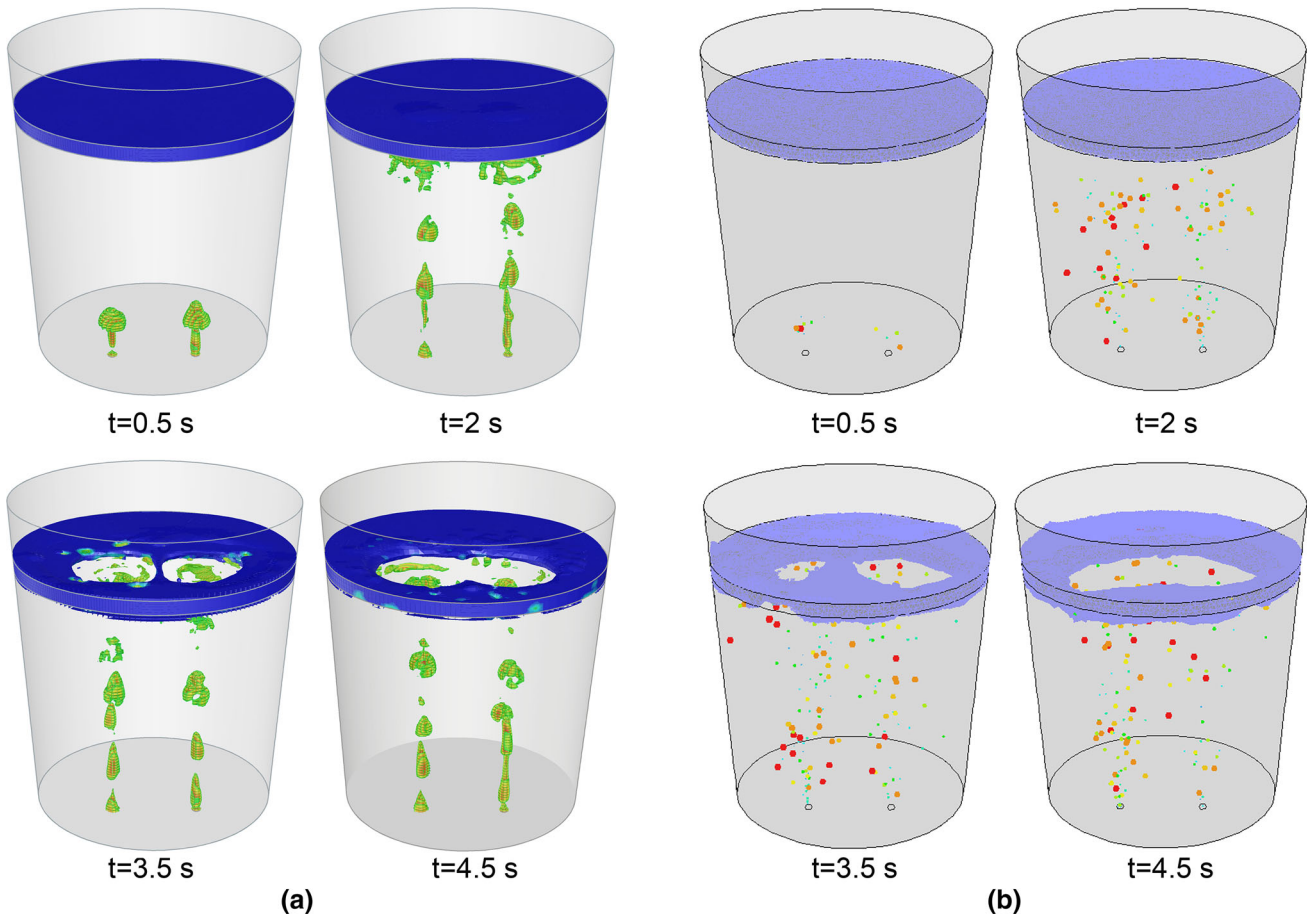
Fig. 4—The argon gas floating and slag eye formation process at the beginning predicted by: (*a*) VOF model, (*b*) DPM model.

Figures 5(a) and (b) show the predicted slag-steel interface viewed from the bottom side of the ladle. As it can be seen from these figures, the slag-steel interface predicted by the DPM model is more fluctuant and uneven. Accordingly, the predicted slag-steel interfacial area by the VOF and DPM models will be different. The variation of the interfacial area with time in Figure 5(c) illustrates that the slag-steel interfacial area predicted by the DPM model is larger than that simulated by the VOF model. Figures 5(d) and (e) display the turbulent intensity in the two-plug section plane predicted by the two different CFD models. At the gas inlets, the turbulence predicted by the VOF model is stronger. Above the gas inlets, the DPM model predicts stronger turbulence than the VOF model. This is in good agreement with the turbulent kinetic energy prediction in the water model shown in Figure 2(b). Figures 5(g) and (h) display the velocity vector at the section plane of the two plugs by the two different CFD models. It can be observed that along the gas plume, the liquid velocity predicted by the VOF model is larger, while at the free surface, the variation of the velocity directions predicted by the DPM model is more intensive. The velocity near the ladle wall predicted by DPM model is larger than that simulated by the VOF model.

The mass transfer coefficients in each mesh cell, as well as the volume-average mass transfer coefficient in the ladle, can be calculated from the simulated turbulent parameters based on Eq. [18]. Figure 5(f) shows the volume-average mass transfer coefficient in steel. The mass transfer coefficients in steel predicted by the VOF and DPM models have no significant difference.

C. *Effects of the Free Surface Setup*

In most of the previous modeling attempts, the interface between the melt and the top gas, which is known as free surface, is approximated with a flat and frictionless wall to simplify the simulation of industrial gas-stirred ladles. However, the error of this assumption is quite large, as verified in Section III. A. In this section, the DPM model was applied to compare the difference of the turbulent flow and the slag-steel phase interaction in gas-stirred ladles between simulations with flat/non-flat free surface. The geometry and meshes shown in Figure 1 are for the non-flat surface conditions, in which a free space above the slag is filled with air. While for the flat surface condition, changes are made in the mesh geometry: (i) no free space exists above the slag, (ii) pressure outlet boundary condition is used at the top surface of the slag, where the argon bubbles are allowed to escape.

The computed turbulent kinetic energy distributions of the free surface and the section plane of two plugs are
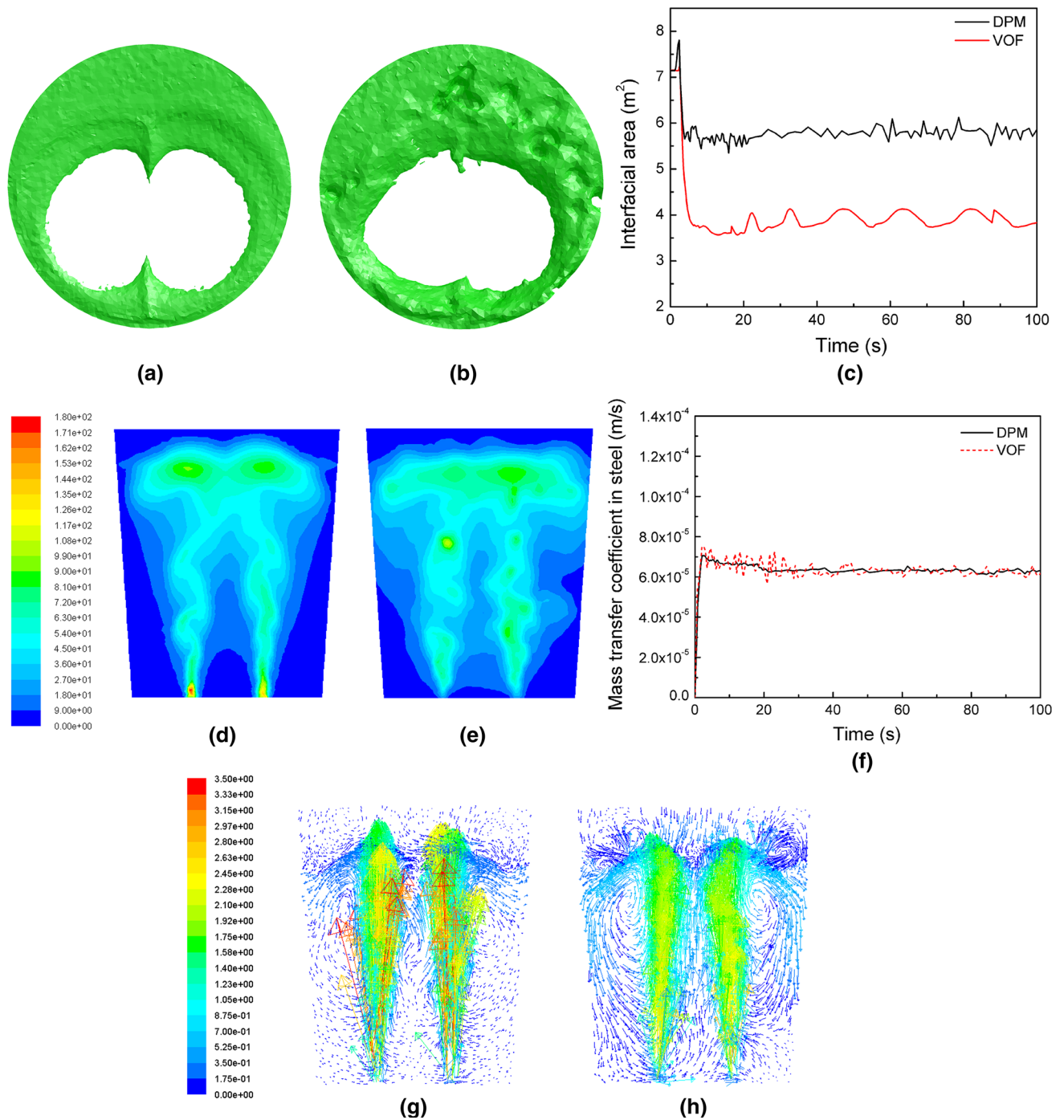
Fig. 5—(a, b) Predicted slag-steel interface shape by VOF model and DPM model, respectively; (c) the variation of the slag-steel interfacial area with time; (d, e) predicted turbulent intensity (unit: 1/100) at the section plane of the two plugs by VOF model and DPM model, respectively; (f) the variation of the mass transfer coefficient in steel with time; (g, h) the velocity vectors (unit: m/s) at the section plane of the two plugs by VOF model and DPM model, respectively.

illustrated in Figure 6. The gas flow rate is 24 L/s and the slag layer thickness is 150 mm. When a flat free surface is assumed, the melt surface is flat and no spouts can be predicted. While the non-flat free surface setup allows the raised spouts and fluctuant melt surface to form. The spout eyes are eccentric and asymmetric with respect to the circular free surface in Figures 6(a) and

(b). This is because the gas injecting location at the bottom are off the symmetric plane of the ladle. Another obvious discrepancy is that the turbulence intensity in the spout eye region of the non-flat free surface is larger than that of the flat free surface setup. Turbulence kinetic energy dissipation in the spout eye region is the primary kinetic energy sink in the ladle. When a flat free
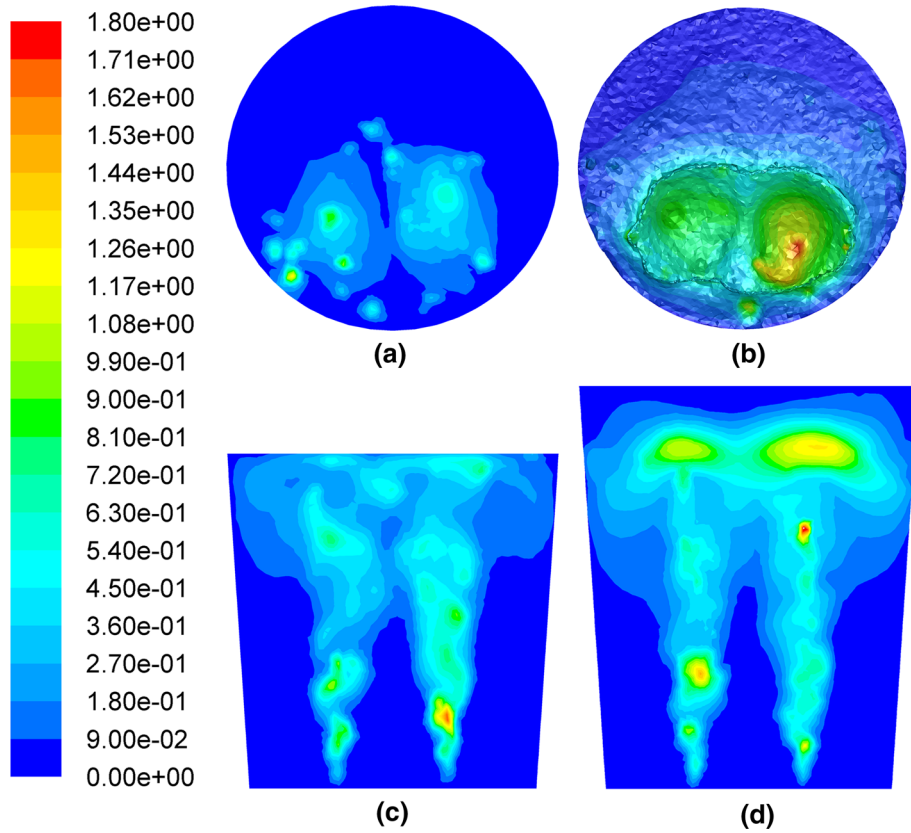
Fig. 6—Predicted turbulent kinetic energy at the melt surface for: (*a*) flat free surface, (*b*) non-flat free surface; and at the section plane of two plugs for: (*c*) flat free surface, (*d*) non-flat free surface (unit: m^2/s^2).
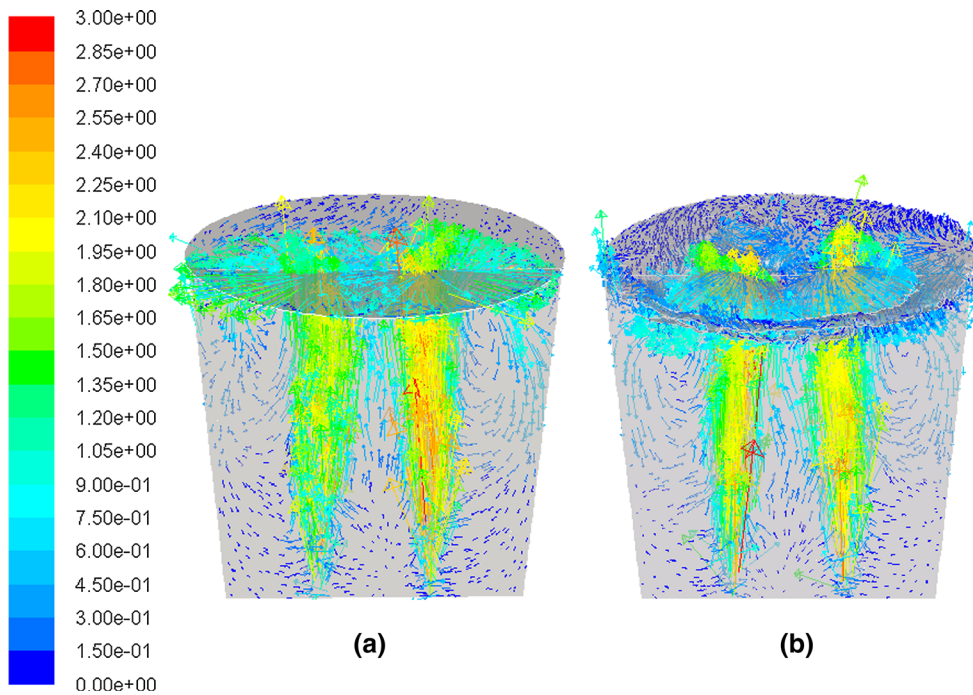

Fig. 7—Calculated velocity vectors of the melt surface and the section plane of the two plugs for: (*a*) flat free surface, (*b*) non-flat free surface (unit: m/s).
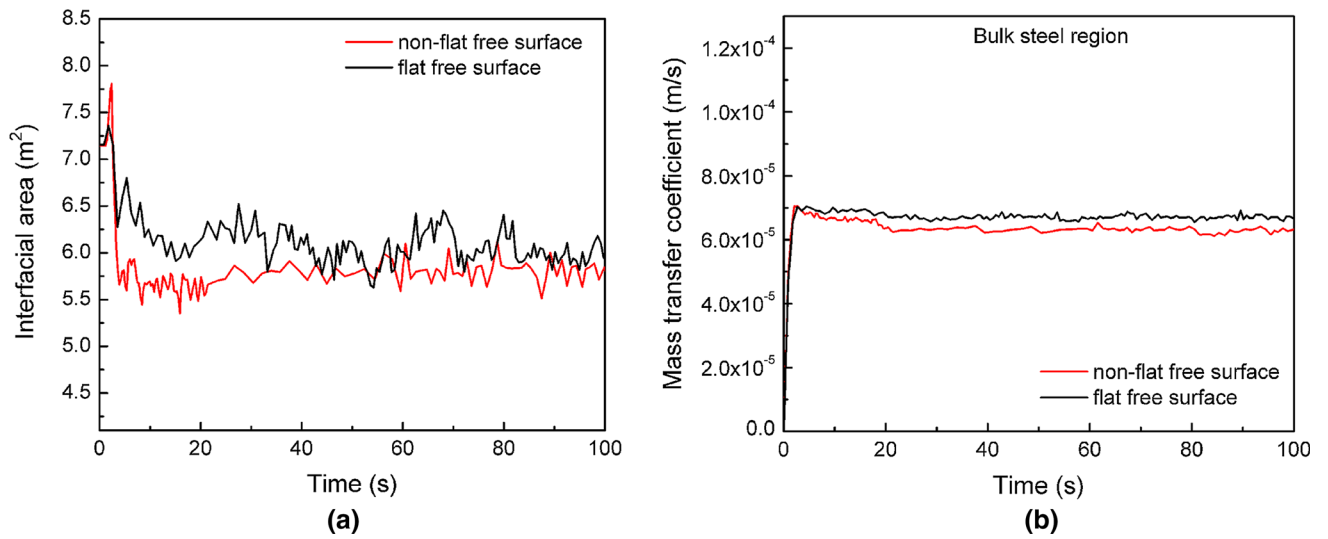
Fig. 8—Predicted variation of (*a*) slag-steel interfacial area, and (*b*) mass transfer coefficient in steel with flat/non-flat free surface.
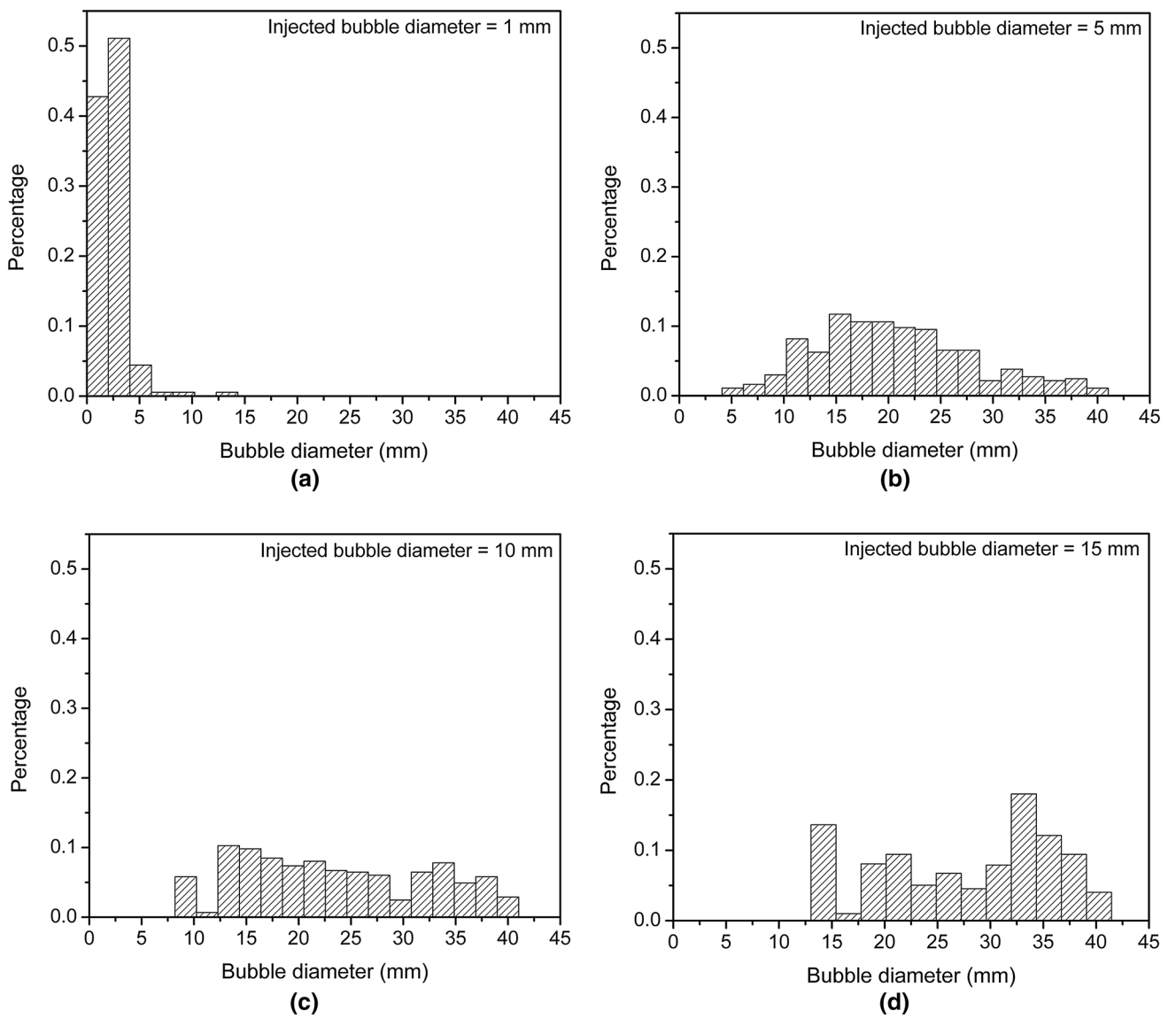
Fig. 9—Bubble size statistics in the ladle at *t* = 100 s with different injected bubble diameters: (*a*) 1 mm, (*b*) 5 mm, (*c*) 10 mm, (*d*) 15 mm.
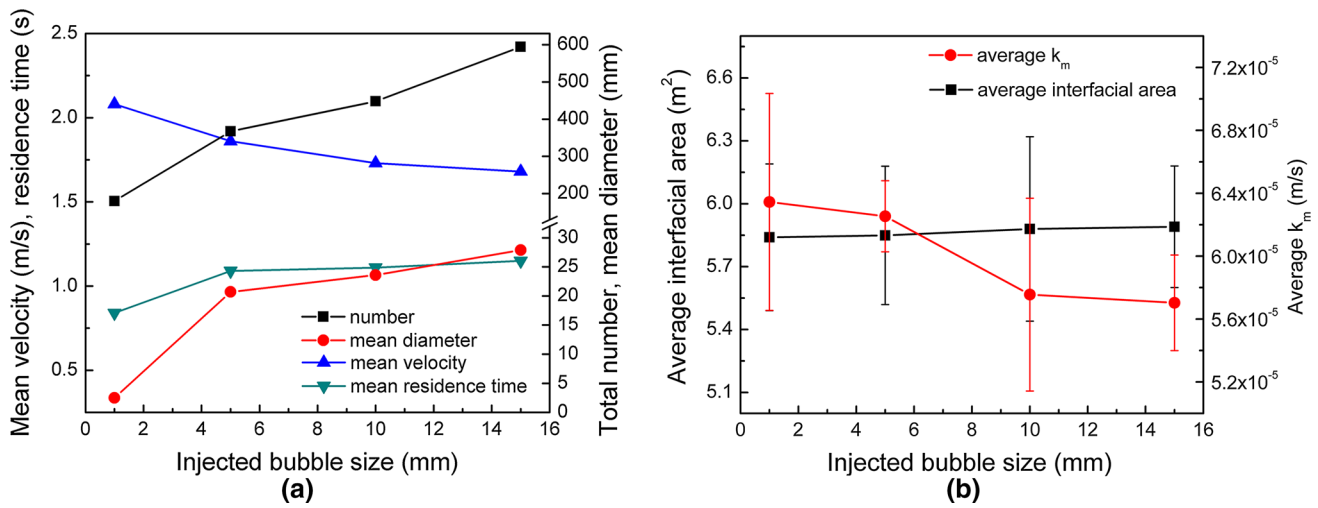
Fig. 10—(a) The average values of bubble characteristics in the ladle at t = 100 s, (b) the predicted average slag-steel interfacial area and mass transfer coefficient in steel with different injected bubble sizes.
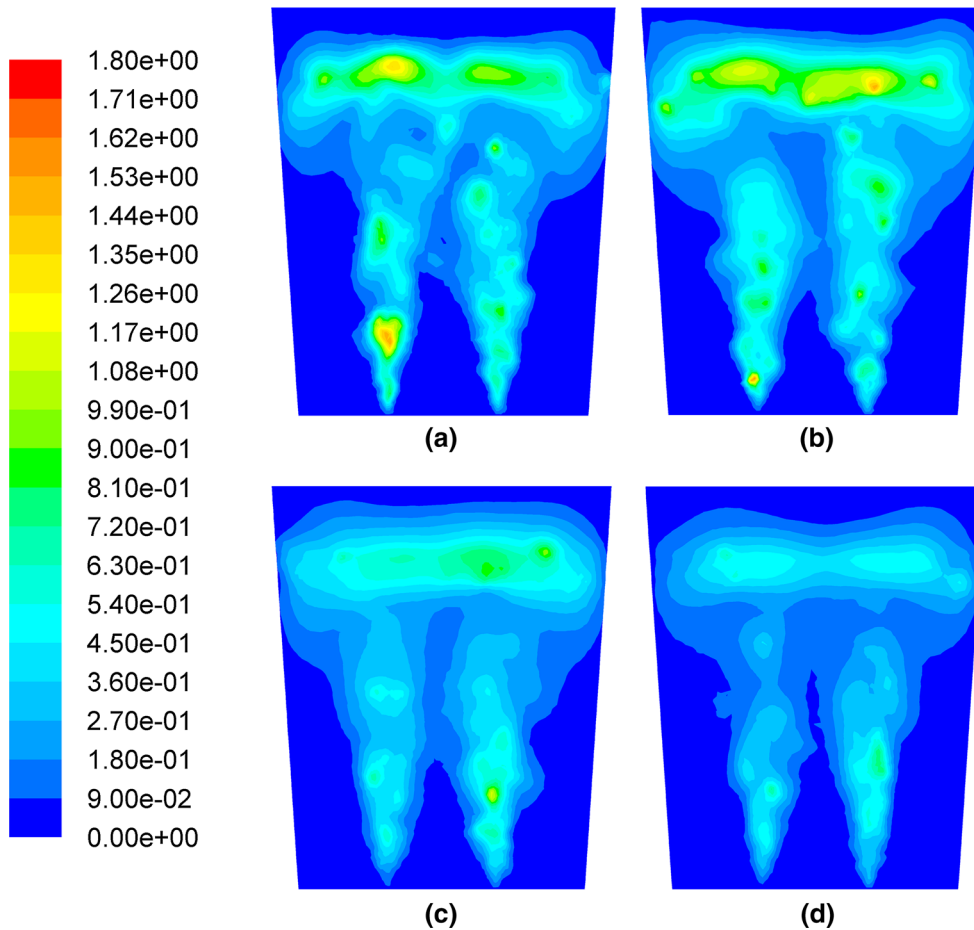

Fig. 11—Predicted turbulent kinetic energy at the section plane of two plugs with different injected bubble diameters: (a) 1 mm, (b) 5 mm, (c) 10 mm, (d) 15 mm (unit: m^2/s^2).

surface is applied, the energy dissipation due to surface wave formation is ignored, which will result in an overestimation of the overall kinetic energy in the ladle.

Figure 7 shows the computed velocity vectors of the melt surface and the section plane of two plugs with a flat/non-flat free surface. It can be seen that the
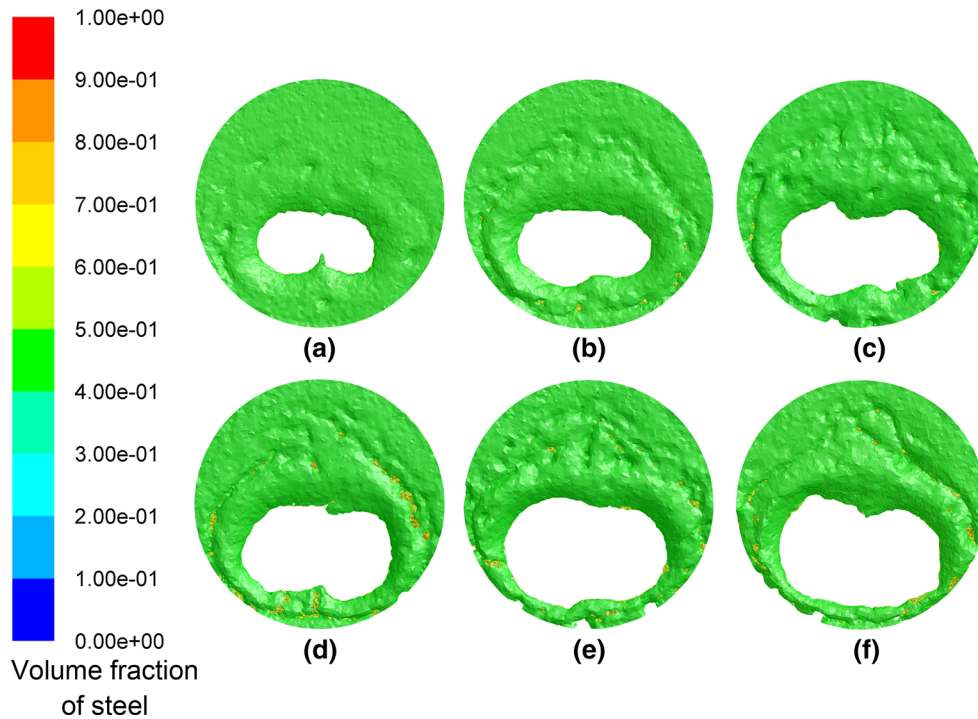
Fig. 12—Predicted slag-steel interface shape under different gas stirring rates: (*a*) 4 L/s, (*b*) 8 L/s, (*c*) 12 L/s, (*d*) 16 L/s, (*e*) 20 L/s, (*f*) 24 L/s.

circulatory flow patterns in steel are similar in both conditions, while the velocity of the melt surface shows significant differences. When a flat free surface is applied, the upwelling steel velocity in the slag eyes will be sharply redirected to radial direction, as displayed in Figure 7(a). For the non-flat free surface condition, the raised spouts in this region provide an opportunity for the upward liquid velocity to be redirected radially in a more gradual trend.

Figure 8 compares the slag-steel interfacial area and the mass transfer coefficient in steel predicted with flat/non-flat free surface conditions. Both the interfacial area and the mass transfer coefficient in the molten steel simulated with the flat free surface are slightly larger than that simulated with the non-flat free surface condition. Under the flat free surface condition, the slag surface deformation is ignored; the slag layer would become much thicker after the slag eyes are formed, and thus the contact area between the slag and the steel would be larger compared to that of the non-flat surface condition. The reason for larger k_m is that the flat free surface assumption over-predicts the circulatory flow in steel due to the underestimated turbulence losses in the spout eyes. From the above comparison, the errors caused by the flat free surface assumption are quite considerable. Therefore, to ensure the simulation accuracy of the gas-stirred ladles, the fluctuation of the top melt surface should be taken into account.[14]

D. *Effects of the Injected Bubble Size*

In a gas-stirred ladle, different bubble diameters can be obtained by changing the structure of porous plugs or the diameter of the nozzle. The effects of different bubble diameters on the phase interaction and fluid flow in gas-stirred ladles were studied. The gas flow rate is 24 L/s and the slag layer thickness is 150 mm. Figure 9 shows the calculated size distribution of the gas bubbles in the ladle at $t = 100$ seconds with the initial bubble diameter increasing from 1 to 15 mm. It can be seen that the bubble size statistics are significantly over the injected bubble diameter, which is the result of bubble collision and coalescence phenomena during the bubble floating process. The floating bubble is assumed to break into two bubbles with equivalent mass when the bubble diameter is over the critical diameter of 40 mm.

Figure 10(a) summarizes the average values of bubble characteristics in the ladle. With the injected bubble size increasing, the average diameter of the bubbles residing in the ladle enlarges from 2.5 to 27.9 mm, while the average velocity of bubbles decreases, which can affect the turbulent flow rate of the melt. As a result of reduced bubble velocity, the average residence time of bubbles increases, and the instantaneous amount of the bubbles existing in the ladle becomes larger. The turbulent kinetic energy distribution with different injected bubble size is illustrated in Figure 11. It can be observed that as the injected bubble size increases, the turbulence in the ladle becomes weaker.

Figure 10(b) presents the average slag-steel interfacial area and the mass transfer coefficient in steel with different initial bubble sizes. With the enlargement of the injected bubble size, the average slag-steel interfacial area slightly increases, while the mass transfer coefficient in steel decreases. This is because the smaller bubbles generate a much more uniform gas distribution than the larger ones, which produce stronger turbulence intensity in the ladle. Similarly, Zhang et al.[4] demonstrated that
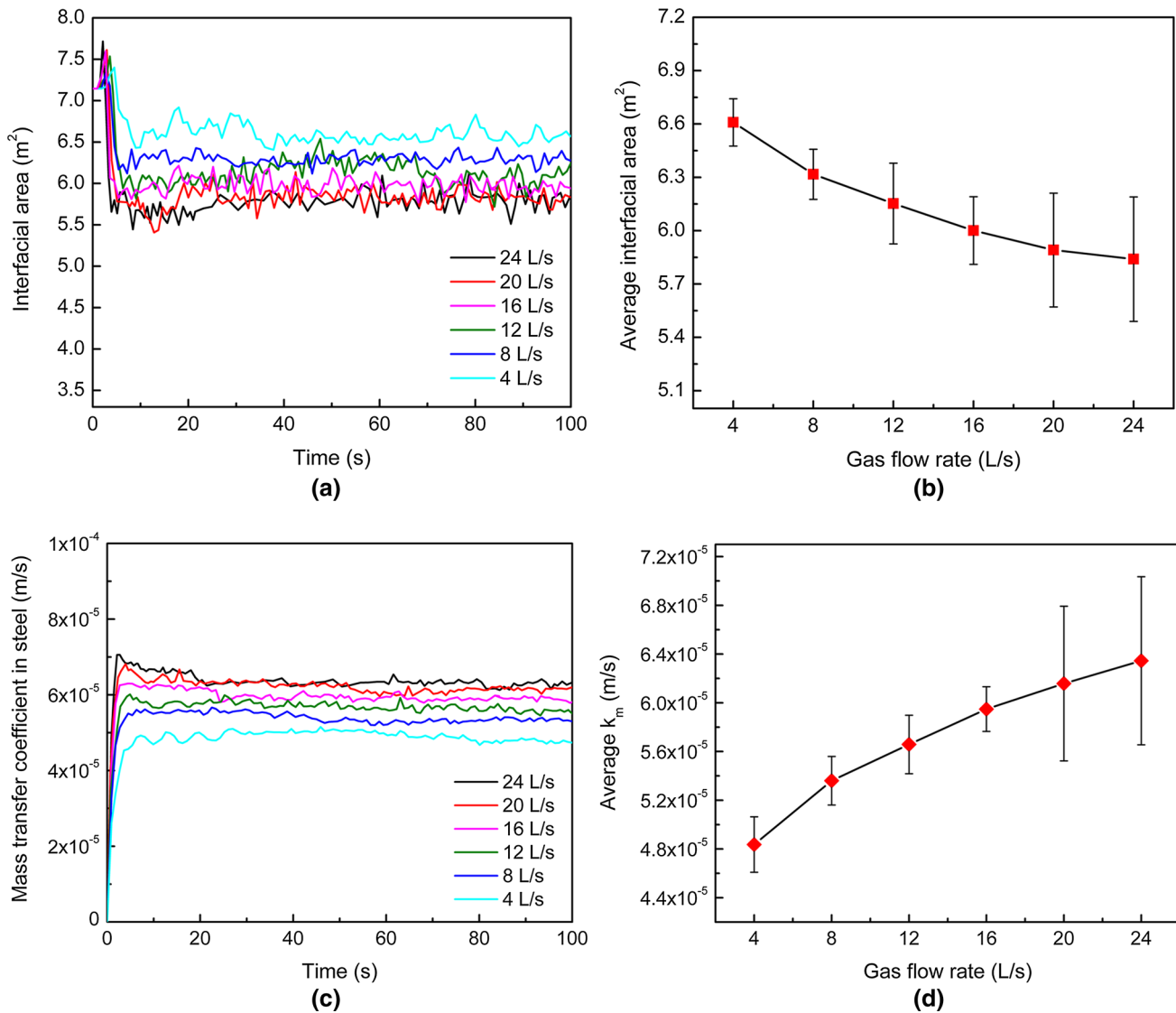
Fig. 13—(*a*) The variation of predicted slag-steel interfacial area with time, (*b*) the average values of slag-steel interfacial area, (*c*) the variation of mass transfer coefficient in steel with time, and (*d*) average values of k_m under different gas stirring rates.

the gas plume formed by 1 mm bubbles is wider than that by 15 mm bubbles in gas-stirred ladles with one-centered bottom plug. Above comparison indicates that finer bubble injection is more favorable for good stirring conditions and thus helps to promote the ladle refining efficiency.

E. *Effects of the Gas Flow Rate*

The effects of argon gas flow rate on the slag-steel phase interaction and the fluid flow characteristics are presented in this section. When the gas stirring rate increases from 4 to 24 L/s, the injected bubble size determined by Eq. [20] only shows a slight increase (from 1 to 2.2 mm). Thus in this part of the study, in order to investigate the effects of gas flow rate, the influence of the injected bubble size is ignored and the injected bubble diameter is kept 1 mm. The slag layer thickness is 150 mm. The slag-steel interface formed

under different gas flow rates is illustrated in Figure 12. The injected gas causes upwelling steel flow and pushes slag towards the ladle wall, forming open eyes. The higher the gas flow rate, the more the slag is displaced, which leads to bigger eye formation. As displayed in Figure 12, the opening size of the slag eyes rapidly enlarges with the increased gas flow rate, and the contact area between the slag and the steel would decrease.

Figure 13(a) shows the variation of the slag-steel interfacial area with time. It can be seen that the size of the interfacial area is constantly changing with time, demonstrating the transient fluctuant behavior of the slag layer. As gas stirring rate increases from 4 to 24 L/s, the time-averaged slag-steel interfacial area slightly decreases by less than about 11 pct, as displayed in Figure 13(b). This is because the opening area of the slag eyes increases with the increase in the gas flow rate, which has been illustrated through Figure 12. When the gas stirring rate approaches 20 L/s, the standard
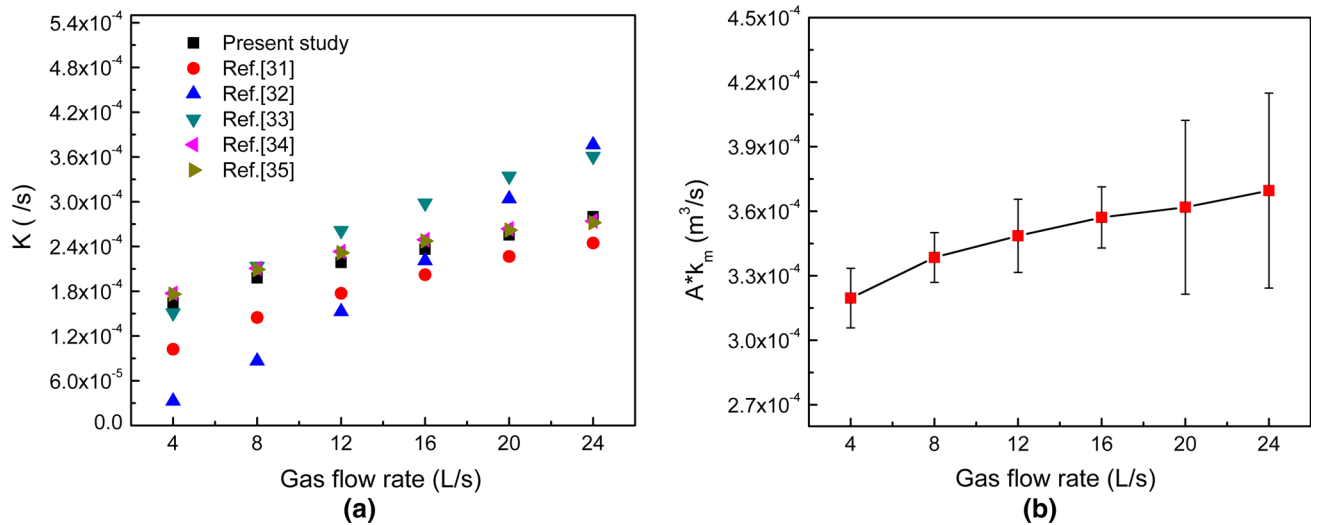
Fig. 14—(a) The comparison of the mass transfer rate predicted within this study against those calculated from the empirical correlations in Ref. [33] to [37], (b) the volumetric mass transfer coefficient under different gas flow rates.
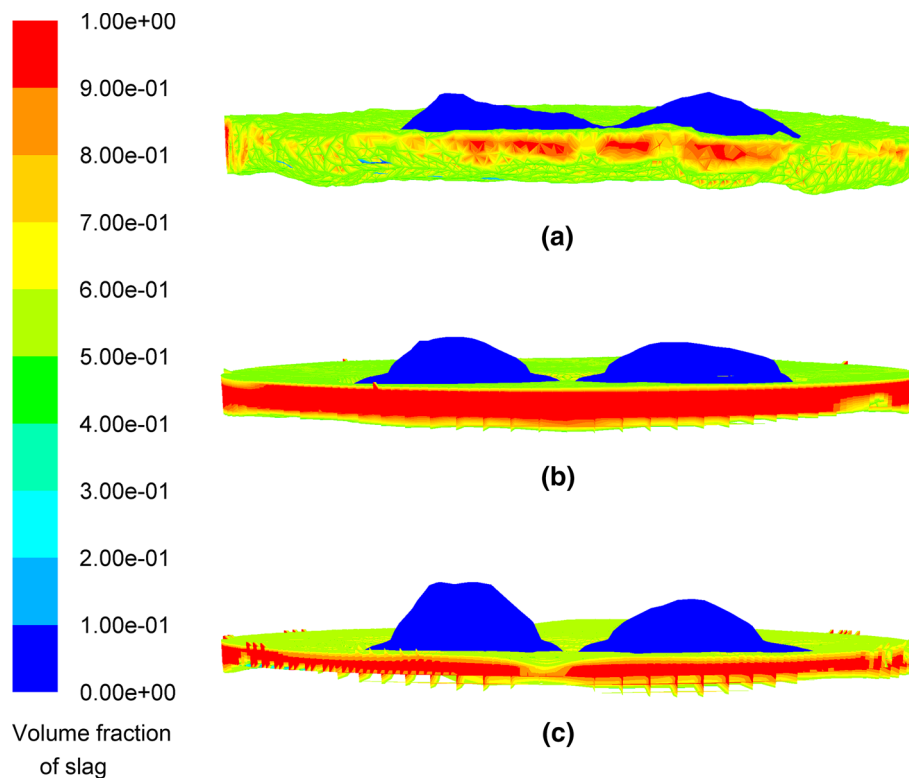

Fig. 15—The slag layer and spout wave for different slag layer thicknesses: (a) 150 mm, (b) 125 mm, (c) 100 mm.

deviation of the interfacial area increases remarkably, which indicates that the slag layer would fluctuate more violently under higher gas stirring rate conditions.

Figures 13(c) and (d) display the predicted mass transfer coefficient in steel. The mass transfer coefficient in the steel phase improves obviously as the gas stirring rate increases. Jonsson *et al.*[32] have shown in their model simulations that the desulfurization rate mainly depends on the transfer rate of sulfur from the steel to the slag-steel interface. From the above results, higher gas flow rate can promote the transport of species from the bulk steel to the slag-steel interface, providing more favorable conditions for the slag-metal reactions.

Many empirical correlations[33–37] have been obtained from experimental data to calculate the mass transfer rate, K, in gas-stirred ladles. The correlation between K and k_m can be expressed as[38]
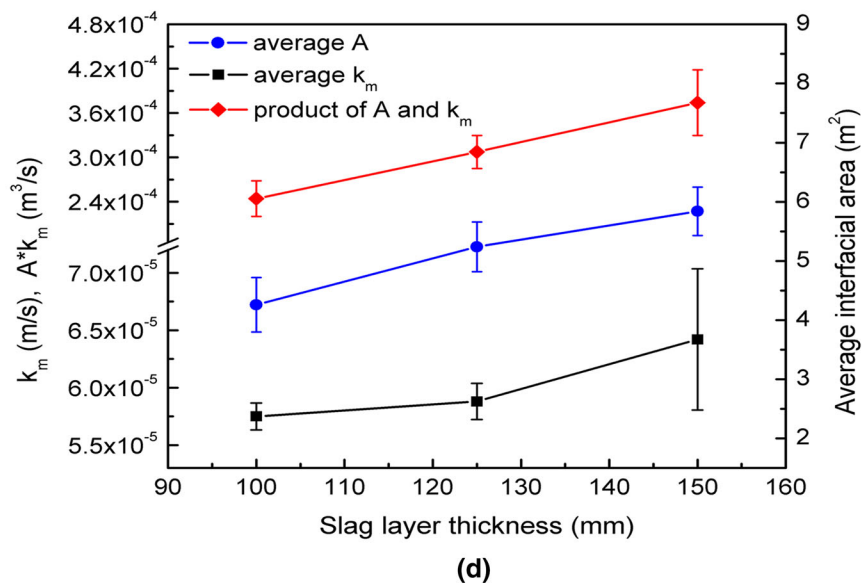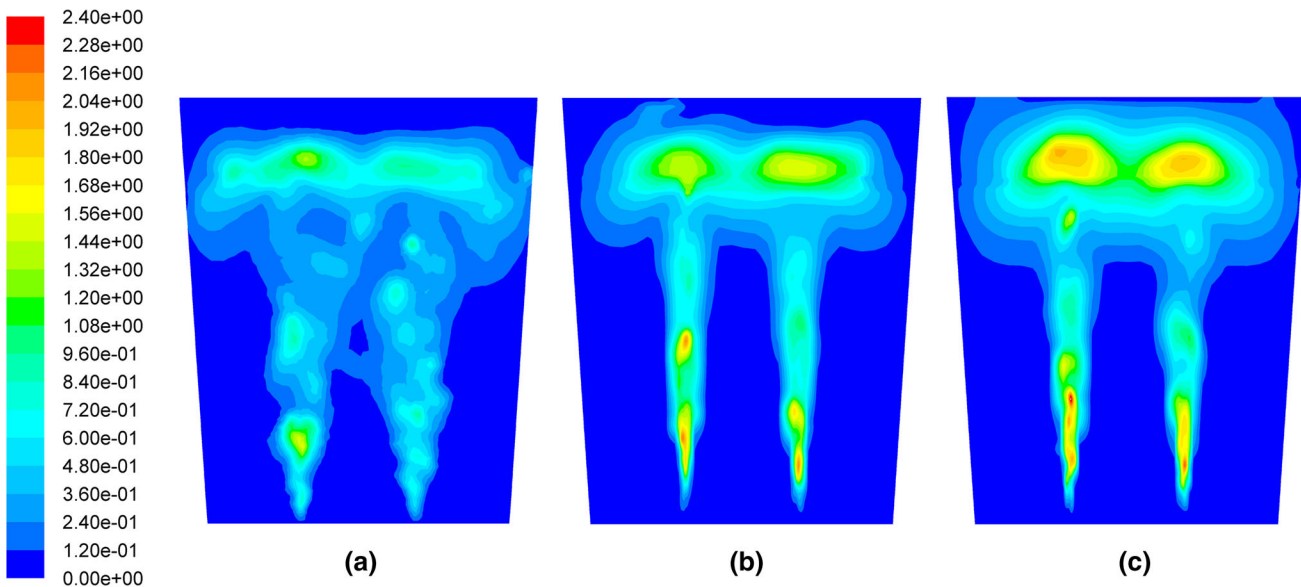
Fig. 16—The turbulent kinetic energy contour at the section plane of two plugs for different slag layer thicknesses: (*a*) 150 mm, (*b*) 125 mm, (*c*) 100 mm, (unit: m²/s²); (*d*) the average slag-steel interfacial area, mass transfer coefficient in steel, and volumetric mass transfer coefficient.

$$K = k_m \frac{A}{V}, \qquad [21]$$

where A is the slag-steel interfacial area, and V is the steel volume. In order to further verify the current mathematical model, a quantitative comparison of the mass transfer rate predicted in this study against those calculated via the empirical correlations[33–37] is shown in Figure 14(a). The result in the present study appears to capture the influence of the gas flow rate on the mass transfer rate, and to be comparable with the empirical correlations.

The volumetric mass transfer coefficient (Ak_m) is presented in Figure 14(b). It can be seen that the volumetric mass transfer coefficient still improves although the slag-steel interface gets smaller as the gas stirring rate increases. Therefore, the desulfurization

rate can be improved through properly increasing the gas stirring rate.

F. *Effects of the Slag Layer Thickness*

The effects of the slag layer thickness on the fluid flow and the slag-steel phase interaction are also investigated in this study. The gas stirring rate is kept 24 L/s and the slag layer thickness varies from 100 to 150 mm. Figure 15 illustrates the slag layer and the spout wave for different slag layer thicknesses. It can be observed that with a thinner slag layer, the upwelling steel flow tends to push the slag easier, producing higher spouts and larger slag eyes. In addition, the turbulence kinetic energy dissipation at the free surface, particularly near the spout eyes, is increased, as shown in Figures 16(a) and (c). As a result, the turbulence intensity in the bulk

steel region would become weaker, and thus, the mass transfer coefficient in steel is decreased.

The average slag-steel interfacial area, the mass transfer coefficients in the molten steel, and the volumetric mass transfer coefficients are displayed in Figure 16(d). With the reduction of the slag layer thickness, both the slag-steel interfacial area and the mass transfer coefficient in the molten steel decrease. Accordingly, the volumetric mass transfer coefficient is also decreased. This indicates that a thinner slag layer does not provide a fast desulfurization reaction rate.[2]

IV. CONCLUSIONS

The Euler-Euler and Euler-Lagrange modeling approaches have been developed in this study to simulate the fluid flow characteristics in water model and gas-stirred ladle systems. The results in terms of fluid flow and phase interaction simulated by these two models were analyzed and compared in detail. The comparison between the modeling and experimental results of the water model shows that the Euler-Lagrange approach is more accurate than the Euler-Euler approach to simulate the fluid flow characteristics in gas-stirred ladles.

The effects of the free surface condition, the injected bubble size, the gas stirring rate, and the slag layer thickness on the slag-steel interaction and the mass transfer coefficient in steel were also studied by using the Euler-Lagrange approach. The simulation results indicate the following:

(1) A flat free surface assumption causes an over-prediction of the circulatory flow in the steel as a result of the underestimated turbulence losses in the spout eye region.
(2) With the enlargement of the injected bubble size, turbulence in the ladle would become weaker and consequently the mass transfer coefficient in steel is decreased.
(3) As the gas stirring rate increases, the mass transfer coefficient in the molten steel becomes larger, and conversely, the slag-steel interfacial area gets smaller, while the volumetric mass transfer coefficient still increases.
(4) When the slag layer thickness is decreased, both the slag-steel interfacial area and the mass transfer coefficient in the molten steel decrease. The simulation results indicate that injecting finer bubbles, properly increasing the gas stirring rate and the slag layer thickness can provide a higher refining efficiency in the ladle metallurgical furnace.

ACKNOWLEDGMENTS

REFERENCES

1. W.T. Lou and M.Y. Zhu: *ISIJ Int.*, 2015, vol. 55, pp. 961–69.
2. Q. Cao, A. Pitts, and L. Nastac: *Ironmak. Steelmak.*, 2016, vol. 12, pp. 1–8.
3. U. Singh, R. Anapagaddi, S. Mangal, K.A. Padmanabhan, and A.K. Singh: *Metall. Mater. Trans. B.*, 2016, vol. 47B, pp. 1804–16.
4. G. Irons, A. Senguttuvan, and K. Krishnapisharody: *ISIJ Int.*, 2015, vol. 55, pp. 1–6.
5. D. Guo and G.A. Irons: *Metall. Mater. Trans. B.*, 2000, vol. 31B, pp. 1458–64.
6. P. Dayal, B. Kristina, B. Johan, and S.C. Du: *Ironmak. Steelmak.*, 2016, vol. 33, pp. 454–64.
7. H.P. Liu, Z.Y. Qi, and M.G. Xu: *Steel Res. Int.*, 2011, vol. 82, pp. 440–58.
8. K. Krishnapisharody and G.A. Irons: *Metall. Mater. Trans. B.*, 2006, vol. 37B, pp. 763–72.
9. M. Al-Harbi, H.V. Atkinson and S. Gao: *Proc. XIth MCWASP Conf.*, 2006, pp. 1089–96.
10. S.M. Pan, Y.H. Ho, and W.S. Hwang: *J. Mater. Eng. Perform.*, 1997, vol. 6, pp. 311–18.
11. S.T. Johansen and F. Boysan: *Metall. Mater. Trans. B.*, 1988, vol. 19B, pp. 755–64.
12. D. Mazumdar and R.I. Guthrie: *ISIJ Int.*, 1994, vol. 34, pp. 384–92.
13. G.J. Chen, S.P. He, and Y.G. Li: *Metall. Mater. Trans. B.*, 2017, vol. 48B, pp. 2176–86.
14. S.W.P. Cloete: *Doctoral dissertation*, Stellenbosch University, 2008.
15. W.T. Lou and M.Y. Zhu: *Metall. Mater. Trans. B.*, 2013, vol. 44B, pp. 1251–63.
16. ANSYS FLUENT 17.1: *User's Guide*. ANSYS, Inc.
17. S.W.P. Cloete, J.J. Eksteen, and S.M. Bradshaw: *Prog. Comput. Fluid Dyn.*, 2009, vol. 9, pp. 345–56.
18. J.P. Zhang, Y. Li, and L.S. Fan: *Powder Technol.*, 2000, vol. 112, pp. 46–56.
19. S. Cloete, J.E. Olsen, and P. Skjetne: *Appl. Ocean Res.*, 2009, vol. 31, pp. 220–25.
20. J.L. Xia, T. Ahokainen, and L. Holappa: *Scand. J. Metall.*, 2001, vol. 30, pp. 69–76.
21. P. Sulasalmi, A. Krn, T. Fabritius, and J. Savolainen: *ISIJ Int.*, 2009, vol. 49, pp. 1661–67.
22. Y.H. Liu, H. Zhu, and L.P. Pan: *Adv. Mech. Eng.*, 2014, vol. 6, p. 834103.
23. B.K. Li, H. Yin, C.Q. Zhou, and F. Tsukihashi: *ISIJ Int.*, 2008, vol. 48, pp. 1704–11.
24. K. Yonezawa and K. Schwerdtfeger: *Metall. Mater. Trans. B.*, 1999, vol. 30B, pp. 411–18.
25. L.M. Li, Z.Q. Liu, M.X. Cao, and B.K. Li: *JOM.*, 2015, vol. 67, pp. 1459–67.
26. P.J. O'Rourke: Ph.D. Thesis, Princeton University, 1981.
27. L. Nastac, D. Zhang, Q. Cao, A. Pitts and R. Williams: *TMS 2016 Proc.*, 2016, pp. 187–94.
28. W.T. Lou and M.Y. Zhu: *Metall. Mater. Trans. B.*, 2014, vol. 45B, pp. 1706–22.
29. Y.Y. Sheng and G.A. Irons: *Metall. Mater. Trans. B.*, 1995, vol. 26B, pp. 625–35.
30. L.M. Li and B.K. Li: *JOM.*, 2016, vol. 68, pp. 2160–69.
31. Q. Cao and L. Nastac: *TMS 2018 Annual Meeting & Exhibition, Proc."CFD Model. Simul. Mater. Process." Symp.*, ed. by L. Nastac, K. Pericleous, A. S. Sabau, L. Zhang, B. G. Thomas, Phoenix, AZ, 11–15 March, 2018.
32. L. Jonsson, S. Du, and P. Jönsson: *ISIJ Int.*, 1998, vol. 38, pp. 260–67.
33. J. Peter, K.D. Peaslee, D.G. Robertson and B.G. Thomas: *AISTech Conf.*, Charlotte, NC, 2005, vol. 1, pp. 959–67.
34. K.J. Graham and G.A. Irons: *Iron Steel Technol.*, 2009, vol. 6, pp. 164–73.

35. A. Harada, N. Maruoka, H. Shibata, and S. Kitamura: *ISIJ Int*., 2013, vol. 12, pp. 2110–17.
36. P.E. Anagbo and J.K. Brimacombe: *Iron Steelmak*., 1988, vol. 11, p. 41.
37. E. Pretorius and H. Oltmann. Desulfurization. Process technology Group-LWB refractories. http://etech.lwbref.com/Downloads/Theory/Desulphurization%20by%20slag%20treatment.pdf, pp. 1–22.
38. S.P. Burmasov, A.G. Gudov, Y.G. Yaroshenko, V.V. Meling, and L.E. Dresvyankina: *Steel Transl*., 2015, vol. 45, pp. 635–39.